

## Remote-sensing-based estimates of the fundamental global water cycle: Annual cycle

Vikram M. Mehta and Andrew J. DeCandis

Center for Research on the Changing Earth System, Columbia, Maryland, USA

Amita V. Mehta

Joint Center for Earth System Technology, University of Maryland, Baltimore County, Baltimore, Maryland, USA

NASA Goddard Space Flight Center, Greenbelt, Maryland, USA

Received 7 December 2004; revised 11 April 2005; accepted 10 August 2005; published 24 November 2005.

[1] The average annual cycle of the atmospheric branch of the fundamental global water cycle (FGWC) was studied with remote-sensing-based precipitation estimates from the Global Precipitation Climatology Project (GPCP; blended microwave-infrared-rain gauge) Version 2 and the Goddard Profiling algorithm (GPROF; passive microwave) Version 6 data sets and overocean evaporation estimates from the Goddard Satellite Surface Turbulent Fluxes Version 2 (passive microwave) data set from 1988 to 2000. Overland evaporation was estimated from the remote-sensing-based precipitation estimates combined with a global evaporation minus precipitation (EmP) data set produced by the Climate Analysis Section of the National Center for Atmospheric Research. Results show that 75% to 85% of the total global evaporation and approximately 70% of the total global precipitation occur over the oceans in each season. In the GPCP-based FGWC estimate, there is a remarkable balance in the interhemispheric import-export of atmospheric moisture in December-January-February and June-July-August. The dominant cross-equatorial atmospheric moisture transports in the atmospheric branch of the FGWC supply a significant amount of moisture to precipitation regions and are from the Northern Hemisphere to the Southern Hemisphere in December-January-February and the Southern Hemisphere to the Northern Hemisphere in June-July-August, with approximately  $3 \times 10^6 \text{ m}^3 \text{ s}^{-1}$  net annual transport from the Southern Hemisphere to the Northern Hemisphere in the GPCP-based FGWC estimate. In the GPROF-based FGWC estimate, there are substantial imbalances in interhemispheric moisture transports that may be attributable to missing data over snow- or ice-covered surfaces, inadequate diurnal sampling, and uncertainties in precipitation estimates especially over land. A quantitative evaluation of these results and comparisons with previous FGWC estimates is not possible without quantitative error estimates on precipitation, evaporation, and EmP estimates. These results show that evaporation, precipitation, and atmospheric moisture transport over the oceans play a very important role in the FGWC and that they should be a significant component in the Global Energy and Water Cycle Experiment and other national and international research programs on the global water cycle.

**Citation:** Mehta, V. M., A. J. DeCandis, and A. V. Mehta (2005), Remote-sensing-based estimates of the fundamental global water cycle: Annual cycle, *J. Geophys. Res.*, *110*, D22103, doi:10.1029/2004JD005672.

### 1. Introduction

[2] The sustainability of life on the Earth depends critically on the availability of freshwater. Any threat to the reliability and sustainability of the freshwater supply clearly deserves focused and urgent attention. The demand for freshwater is increasing in direct response to increasing human population. Meanwhile, the supply of freshwater is decreasing because of pollution and other stresses. Some

projections suggest that rapid increases in demand, coupled with limited supplies, will lead to the development of a global water crisis in a matter of decades, with the precise timing of this crisis uncertain because of a limited knowledge of the world's water resources [Rodda, 1995]. While these problems manifest themselves at the local or regional level, the reservoirs and their catchment areas, which supply water to the local or regional level, are sometimes distributed across province/state or national boundaries. The amounts and frequencies of precipitation which supplies water to these reservoirs are influenced by global-scale, subcontinental-scale, or ocean basin-scale

processes. Therefore addressing such problems requires a global view of the freshwater in the Earth-atmosphere system.

[3] We define the atmospheric branch of the fundamental global water cycle (FGWC) in the Earth system as the primary water cycle between the Northern and Southern Hemispheres because of the hemispheric asymmetry in solar radiation. The FGWC is not well quantified because of paucity of observations, especially over the oceans; however, several previous studies have used the then-available observations to quantify the atmospheric branch of the FGWC. *Peixóto and Oort* [1983], using 10 years' (1964–1973) radiosonde measurements of winds and humidity, estimated the annual-average, cross-equatorial water vapor divergence as 0.11 mm/d from the Southern Hemisphere to the Northern Hemisphere. *Chen and Pfaendtner* [1993] compared global precipitation estimates for 1978–1979 from the High-Resolution Infrared Sounder 2/Microwave Sounding Unit (HIRS2/MSU) with divergence of vertically integrated water vapor transport estimated from the European Centre for Medium-Range Weather Forecasts (ECMWF) Global Data Assimilation System (GDAS) to infer geographical distribution of evaporation. Using winds from the National Meteorological Center (NMC) GDAS for 1979–1992 and HIRS2/MSU precipitation, *Chen et al.* [1994] found that water vapor flux diverged out of boundaries of the Atlantic Ocean sector and converged into the Pacific Ocean sector from the Indian Ocean sector. In an attempt to quantify FGWC using the 2-year HIRS2/MSU precipitation and the 14-year NMC GDAS winds, *Chen et al.* [1995] estimated a net, annual-average water vapor divergence from the Southern Hemisphere to the Northern Hemisphere to be 0.22 mm/d.

[4] Following the above-cited studies, there is a void in FGWC studies in the recent past. Many years' precipitation and evaporation estimates based on satellite remote sensing are now available. The focus of this study is to analyze quantitatively the atmospheric branch of the FGWC, using these precipitation and evaporation estimates as primary data sources.

[5] A variety of satellite-derived precipitation products are available, each with its own strengths and weaknesses. Details of these products can be found in a series of Precipitation Intercomparison Projects (PIP-1, -2, and -3) coordinated by the World Climate Research Program (WCRP) [*Barrett et al.*, 1994; *Smith et al.*, 1998; *Adler et al.*, 2001]. Among these, there are two main categories of precipitation estimates based on (1) infrared radiances measured by geostationary satellites and (2) passive microwave (PMW) radiances measured by polar-orbiting satellites. The infrared-based precipitation estimates, the Geostationary Precipitation Index (GPI), are based on a relatively simple algorithm developed by *Arkin and Meisner* [1987], and are available beginning in 1979 [e.g., *Joyce and Arkin*, 1997]. The longest available, multichannel PMW estimates are retrieved from the Special Sensor Microwave/Imager (SSM/I) beginning in 1987, which have been augmented by passive and active microwave sensors on the Tropical Rainfall Measuring Mission since 1997. Many precipitation products based on SSM/I are available with varying degrees of complexity in retrieval methods [*Smith et al.*, 1998, and references therein]. A third category

of precipitation estimates is also available which uses a combination of the GPI- and PMW-based precipitation products blended with rain gauge measurements over land [e.g., *Huffman et al.*, 1997]. These combined precipitation estimates exploit the full diurnal sampling of the GPI while using more accurate precipitation rates from PMW radiances.

[6] Several previous studies suggest that, in general, PMW-based instantaneous precipitation estimates are more accurate compared to either the GPI or combined precipitation estimates, but combined precipitation products are more representative of time-averaged precipitation because of their superior diurnal sampling [*Bauer et al.*, 1998, and references therein]. Moreover, the PIP-2 and PIP-3 studies have pointed out that the range of differences among various precipitation products is large (~30%). Therefore it is likely that characteristics of average precipitation climatology and variability may be quantitatively different in these types of remote-sensing-based estimates. In the present study, we used two precipitation products: (1) a blended product from the Global Precipitation Climatology Project (GPCP), which is derived from a combination of GPI-SSM/I-rain gauge products, and (2) a physically retrieved PMW product from Goddard Profiling algorithm (GPROF) derived from SSM/I measurements with the aid of hydrometeor profiles from a cloud resolving model, which is also currently used in retrieving precipitation from the TRMM Microwave Imager (TMI).

[7] Remote-sensing-based evaporation estimates over global oceans date back to the first SSM/I radiometer launched in 1987, while in situ estimates based on ship and buoy reports, dating back to 1960, are found in the COADS data set. The studies by *Chou* [1993], *Chou et al.* [1995, 1997], *Schlüssel et al.* [1995], *Atlas et al.* [1996], *Schlüssel* [1996], *Clayson et al.* [1996], *Clayson and Curry* [1996], and *Schulz et al.* [1997] have described how evaporation over ocean can be obtained from PMW measurements through first-order surface turbulence closure schemes. Three of these schemes have been used to produce global oceanic evaporation data sets, i.e., (1) Goddard Satellite Surface Turbulent Flux Version 2 (GSSTF2), (2) the Clayson and Curry scheme, and (3) the Schulz and Schlüssel scheme. Of these three available, remote-sensing-based, overocean evaporation estimates, the GSSTF2 evaporation estimates are available for the longest period, i.e., beginning in 1987, and the Schulz et al. data set has data quality and spurious retrieval problems (see, e.g., *Sohn et al.* [2004] for a detailed comparison). Moreover, *Chou et al.* [2003] have compared the GSSTF2 overocean evaporation with four other evaporation data sets and concluded that the GSSTF2 evaporation estimates are likely to be more realistic than the other four. Therefore we use GSSTF2 evaporation estimates over global oceans in the present study. Unlike the overocean evaporation estimates, however, there are no global, gridded, observations-based evaporation estimates available over land regions to date. Following *Chen and Pfaendtner* [1993], we estimated evaporation over land by combining remote-sensing-based precipitation estimates with the evaporation minus precipitation (EmP) estimate produced (D. P. Stepaniak, Vertically integrated mass, moisture heat, and energy budget products derived from the NCEP/NCAR reanalysis, available online

**Table 1.** Acronyms

| Acronym  | Entity   |
|----------|--|
| CRCES    | Center for Research on the Changing Earth System   |
| ECMWF    | European Centre for Medium-Range Weather Forecasts |
| EmP      | evaporation minus precipitation                    |
| FGWC     | Fundamental Global Water Cycle                     |
| GMS      | Geostationary Meteorological Satellite             |
| GOES     | Geostationary Operational Environmental Satellite  |
| GPI      | Geostationary Precipitation Index                  |
| GDAS     | Global Data Assimilation System                    |
| GPCC     | Global Precipitation Climatology Center            |
| GPCP     | Global Precipitation Climatology Project           |
| GPROF    | Goddard Profiling algorithm                        |
| HIRS2    | High-Resolution Infrared Sounder 2                 |
| ITCZ     | intertropical convergence zone                     |
| Meteosat | Meteorological Satellite                           |
| MSU      | Microwave Sounding Unit                            |
| NCAR     | National Center for Atmospheric Research           |
| NCEP     | National Centers for Environmental Prediction      |
| NMC      | National Meteorological Center                     |
| PMW      | passive microwave                                  |
| PIP      | Precipitation Intercomparison Project              |
| SSM/I    | Special Sensor Microwave/Imager                    |
| TOVS     | TIROS Operational Vertical Sounder                 |
| TRMM     | Tropical Rainfall Measuring Mission                |
| TMI      | TRMM Microwave Imager                              |
| WCRP     | World Climate Research Program                     |

at <http://www.cgd.ucar.edu/cas/catalog/newbudgets/>) from the NCEP-NCAR reanalysis by the Climate Analysis Section of the National Center for Atmospheric Research.

[8] The objective of this study was to quantify the average annual cycle and interannual variability of the atmospheric branch of the FGWC (hereinafter referred to only as FGWC), using these precipitation and evaporation estimates. The average annual cycle of the FGWC is described in this paper; interannual variability, including long-term trends, of the FGWC will be described in a forthcoming paper. The following questions are addressed in this paper: What are the rates at which water is processed in each of FGWC components over land and over ocean in the Northern and Southern Hemispheres at seasonal and annual timescales? Are there significant differences in the FGWC estimated from the two types of precipitation estimates? How much net atmospheric freshwater is transported across the equator in the FGWC seasonally and annually? Where are the major sources and sinks of the observed FGWC in each season?

[9] The data sets used in this study are described in section 2, the average annual cycles of precipitation and evaporation patterns are described in sections 3 and 4, respectively. The average annual cycle of atmospheric moisture flux divergence patterns is described in section 5 and the FGWC is described in section 6. Results are discussed and concluding remarks are presented in section 7. Acronyms are defined in Table 1.

## 2. Data

[10] As mentioned earlier, we used monthly precipitation estimates from the GPCP [Huffman *et al.*, 1997; Adler *et al.*, 2003] and the GPROF [Kummerow *et al.*, 1996]. In the GPCP Version 2 product used in the present study, precipitation estimates are obtained by merging precipitation estimates based on low-orbit satellite microwave data,

infrared data from geosynchronous and polar satellites, and surface rain gauge data. The microwave estimates used in this GPCP product are based on SSM/I instruments on the Defense Meteorological Satellite Program satellites. The infrared-based precipitation estimates are obtained from the Geostationary Operational Environmental Satellites (GOES), the Geostationary Meteorological Satellite (GMS), and the Meteorological Satellite (Meteosat). In addition, at middle and higher latitudes over cold surfaces, where the SSM/I estimates are less reliable, precipitation estimates from TOVS instruments onboard NOAA operational satellites are also used together with SSM/I estimates. The higher-accuracy SSM/I precipitation estimates are used to calibrate the more frequent geosynchronous infrared estimates. These satellite estimates are then combined with the surface rain gauge data assembled by the Global Precipitation Climatology Centre (GPCC) to produce final GPCP precipitation estimates [Adler *et al.*, 2003]. The present study focuses on microwave era data from January 1988 to December 2000. The GPCP provides ([http://daac.gsfc.nasa.gov/hydrology/hd\\_precip\\_climatology.shtml](http://daac.gsfc.nasa.gov/hydrology/hd_precip_climatology.shtml)) global, monthly precipitation estimates on a 2.5° longitude by 2.5° latitude grid from January 1979 to the present. The GPCP Version 2 data are present in all grid boxes in each month during the analysis period.

[11] The GPROF precipitation estimates are derived by using an inversion technique applied to multichannel, PMW brightness temperature measurements [Kummerow *et al.*, 1996]. The inversion technique uses the Goddard Cumulus Ensemble model (a nonhydrostatic, microphysical cloud model) to first establish vertical hydrometeor profiles for the precipitation retrievals. Detailed radiative transfer model calculations of upwelling brightness temperatures for different SSM/I channels are carried out from the cloud model profiles. Finally, precipitation is retrieved by matching the probability of SSM/I-derived brightness temperatures and the calculated brightness temperatures according to the Bayes approach [Kummerow *et al.*, 1996]. The GPROF Version 6.0 data set (<ftp://lake.nascom.nasa.gov/data/TRMM/Ancillary/ssmi/>) used in this study are global, monthly precipitation estimates at 0.5° longitude by 0.5° latitude grid spacing from January 1988 to December 2000. It should be noted, however, that a substantial amount of data are missing in the GPROF compared to the GPCP data used in this study. As discussed by Kummerow *et al.* [1996], the GPROF algorithm screens out estimates that are ambiguous because of a cloud-free background land surface and/or a snow- or ice-covered surface. Because of this, GPROF data are available only between 70°S and 70°N (E. Nelkin, personal communication, 2004). It is also important to note that during the 13-year period of this study, the GPROF precipitation estimates from January 1988 to January 1991 are based on single-satellite estimates while more than one satellite estimates are combined beginning in February 1992. There are also missing data for the entire months of March to December in 1990 because of unreliable SSM/I data (E. Nelkin, personal communication, 2004). To analyze impacts, if any, of the missing GPROF data, we replaced missing GPROF data with GPCP data and estimated the FGWC with and without the replaced data. We refer to the GPROF data set in which missing data were replaced by GPCP data as the augmented GPROF data set.

We also estimated the FGWC using the GPCP data with and without the missing GPROF grid boxes. The GPCP data set in which the data missing in GPROF were removed is referred to as the truncated GPCP data set. The four FGWC estimates thus produced are described and discussed in this paper.

[12] We used monthly, overocean evaporation estimates from GSSTF2 ([http://daac.gsfc.nasa.gov/hydrology/hd\\_gsstf2.0.shtml](http://daac.gsfc.nasa.gov/hydrology/hd_gsstf2.0.shtml)) based on SSM/I radiances [Chou *et al.*, 1997]. The GSSTF2 estimates are derived from the SSM/I surface winds and surface air humidity, and air and sea surface temperatures from the NCEP-NCAR reanalysis, using a bulk aerodynamic algorithm based on the surface layer similarity theory. The evaporation estimates are available on a 1° longitude by 1° latitude grid over the oceans. Except in the June-July-August season, the grid boxes where some monthly GSSTF2 data are missing are in the tropics; less than 10% of the monthly data are missing in these grid boxes. Seasonal averages were calculated in these grid boxes using the available data. In the June-July-August season, there are approximately 30–40% monthly data missing in the Arabian Sea, the Bay of Bengal, and the Kuroshio regions. Therefore, out of the possible 39 months in this season during the 13 years analysis period, GSSTF2 data were available in at least 24–28 months to calculate the seasonal average in these regions. Similarly, approximately 30–40% of data are missing in a very narrow region along the tropical Pacific coast of South America in all seasons, but at least 24–28 months of data are available in this region to calculate seasonal averages in all seasons.

[13] EmP from a recently completed (D. P. Stepaniak, Vertically integrated mass, moisture heat, and energy budget products derived from the NCEP/NCAR reanalysis, available online at <http://www.cgd.ucar.edu/cas/catalog/newbudgets/>) recomputation and updating of vertically integrated monthly mean mass, moisture, heat, and energy budget products derived from the NCEP-NCAR reanalysis [Kalnay *et al.*, 1996], combined with the GPCP and GPROF precipitation estimates, was used to estimate evaporation over land regions. This new data set (<http://www.cgd.ucar.edu/cas/catalog/newbudgets/index.html>), produced using the same methodology as Trenberth and Guillemot [1998] and referred to here as S05, spans the period from January 1979 to December 2001, and incorporates TIROS Operational Vertical Sounder (TOVS) reruns in addition to grid corrections implemented by NCEP for reanalysis data covering the period March 1997 through October 2001. The S05 data set underlies (D. Stepaniak, personal communication, 2005) the data used by Trenberth and Stepaniak [2003a, 2003b]. The monthly S05 EmP data were linearly interpolated from its original T42 Gaussian grid to the same 1° longitude by 1° latitude global grid as the remote-sensing-based estimates. The GPCP version 2 data were also linearly interpolated in two dimensions and the GPROF version 6.0 data were averaged in two dimensions to the GSSTF2 1° longitude by 1° latitude grid from January 1988 to December 2000. Following Chen and Pfaendtner [1993], evaporation over land regions was then estimated by arithmetically combining the S05 EmP with the GPCP and GPROF precipitation estimates; two overland evaporation data sets

were thus produced on the 1° longitude by 1° latitude global grid.

### 3. Annual Cycle of Precipitation

[14] The average annual cycle of precipitation over the 1988–2000 period in the GPCP and GPROF data sets is shown in Figure 1. We begin the description of the average annual cycle in the December-January-February season. The intertropical convergence zones (ITCZs) are at their southernmost locations in this season (Figures 1a and 1e) in the Pacific, Atlantic, and Indian Ocean regions. In the Pacific and Atlantic ITCZs, including their extensions over South America, the maximum precipitation is approximately 4 mm/d in both data sets; in the African ITCZ, however, the maximum GPROF precipitation is 8 mm/d compared to 4 mm/d in the GPCP data set and in tropical and southern Africa the GPROF precipitation is 2–4 mm/d more than the GPCP precipitation. Additionally, the Pacific ITCZ is narrower in the meridional direction in the GPROF data set. Over the Indian Ocean, the maximum precipitation in both data sets is 4 mm/d, increasing to 8 mm/d over the Maritime Continent. The Australian monsoon precipitation is approximately the same (4–8 mm/d) in both data sets. In the midlatitude North Pacific and North Atlantic storm track regions, where this is winter season, the maximum precipitation is 4 mm/d in both data sets, but the North Atlantic precipitation maximum is confined near the east coast of North America in the GPROF data set whereas it is elongated to the Arctic in the GPCP data set. The North Pacific maximum is also broader in the northeast direction in the GPCP data set. Subtropical precipitation minima are similar in both data sets.

[15] In the March-April-May period, the ITCZs begin to move northward, the Asian and African monsoons begin to set in, and midlatitude storms begin to weaken in the Northern Hemisphere and strengthen in the Southern Hemisphere. In this season, the Pacific and Atlantic ITCZs have generally similar zonal and meridional extents and amounts of precipitation in the GPCP (Figure 1b) and GPROF (Figure 1f) data sets. The precipitation maximum over equatorial South America is 2–4 mm/d stronger on the western side and 2–4 mm/d weaker on the eastern side in the GPROF data set. Over equatorial Africa, the GPROF precipitation is approximately twice as much (8 mm/d) as the GPCP precipitation and the strong meridional gradient of precipitation in the Sahel is stronger in the GPROF compared to the GPCP data. Over North America and western Europe, the two data sets show generally similar precipitation magnitudes in this season.

[16] In the next three months (June-July-August), precipitation in the Northern Hemisphere tropics increases dramatically as the onsets of the summer monsoons occur in Asia, Africa, and North America. Both the GPCP (Figure 1c) and GPROF (Figure 1g) data sets show these increases. Over the eastern Pacific and Atlantic Oceans, precipitation is twice as much as in the previous season. There is a southward shift in the ITCZ precipitation in the eastern Pacific in GPROF compared to GPCP. GPROF precipitation is approximately 2–4 mm/d in almost the entire North American continent; particularly, the North American monsoon precipitation is more localized and

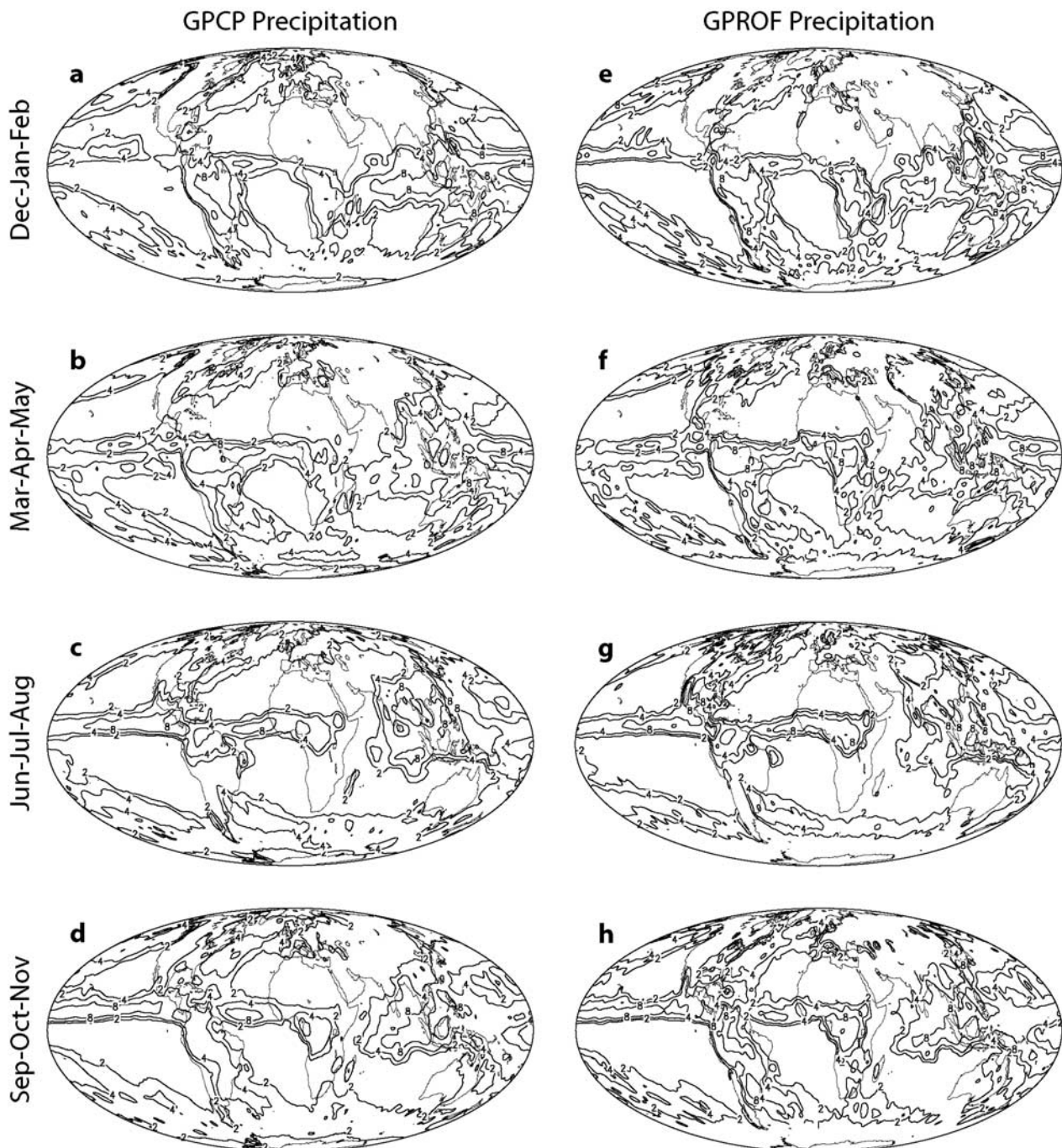


**Figure 1.** Average precipitation during 1988–2000. (a) GPCP; December-January-February. (b) GPCP; March-April-May. (c) GPCP; June-July-August. (d) GPCP; September-October-November. (e) GPROF; December-January-February. (f) GPROF; March-April-May. (g) GPROF; June-July-August. (h) GPROF; September-October-November. Contour values are 2 mm/d, 4 mm/d, 8 mm/d, and 16 mm/d.

almost twice as much in GPROF compared to GPCP. Orographic maxima in the Indian monsoon precipitation are more localized in the GPROF data set compared to the GPCP data set; however, the monsoon precipitation is 2–4 mm/d more in GPCP compared to GPROF. In tropical Africa, the GPROF precipitation is 2–4 mm/d more than the GPCP precipitation. Precipitation in the North Pacific and North Atlantic storm track regions decreases compared to

the previous season (Northern Hemisphere spring) and the Southern Hemisphere storm track precipitation regions become more organized over large spatial scales.

[17] In September-October-November, while precipitation in the Pacific and Atlantic ITCZs is substantially the same in the GPCP (Figure 1d) and GPROF (Figure 1h) data sets, the GPROF ITCZ is shifted southward compared to the GPCP ITCZ. The Northern Hemisphere monsoons weaken

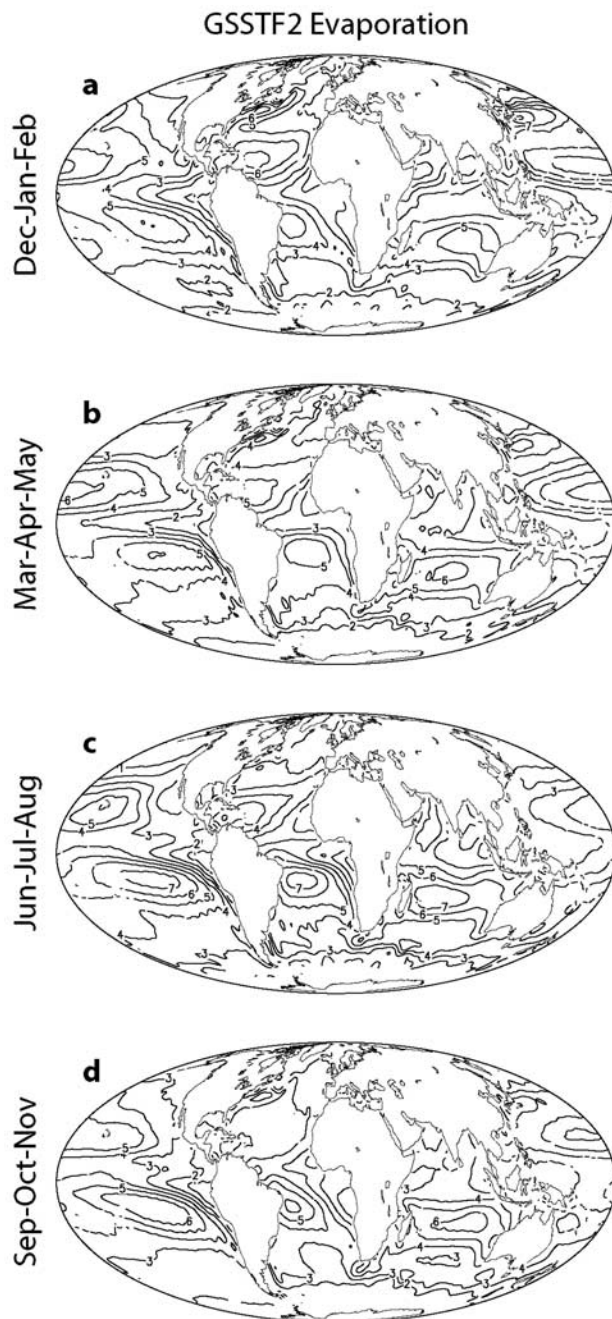


**Figure 2.** Average overocean evaporation during 1988–2000 from GSSTF2. (a) December-January-February, (b) March-April-May, (c) June-July-August, (d) September-October-November. Contour values are 2 mm/d, 3 mm/d, 4 mm/d, 5 mm/d, 6 mm/d, and 7 mm/d.

and precipitation begins to increase in the Northern Hemisphere storm track regions and begins to decrease in the Southern Hemisphere storm track regions. Over Africa and South America, the GPROF precipitation is approximately twice as much as the GPCP precipitation.

[18] In general, the GPCP and GPROF precipitation estimates agree reasonably well over the oceans. There are significant differences between the two, however, over Africa, the Americas, and south Asia. A number of factors

including blended rain gauge data in GPCP, different spatial and temporal samplings, and different retrieval methods in these two precipitation products may be responsible for these differences. The GPROF algorithm differs significantly over land compared to over ocean in terms of SSM/I channel weights [Kummerow *et al.*, 1996]. The GPCP estimates, on the other hand, include rain gauges in the blending over land. Kummerow *et al.* [1996] have compared the GPCP and GPROF precipitation for a sample month and pointed out root-mean-square differences as large as 66% between the two products. While it is beyond the scope of this paper to analyze the causes of these precipitation differences, the FGWCs derived from these two precipitation estimates reflect these differences, as we show in section 5.

#### 4. Annual Cycle of Evaporation

[19] The average evaporation over the oceans from the GSSTF2 data set is shown in Figure 2 for the 1988–2000 period. In December-January-February (Figure 2a), evaporation maxima are over tropical-subtropical oceans in the Northern Hemisphere. There are also intense, localized evaporation maxima over the warm Gulf Stream and Kuroshio currents where cold, dry winds blow from North America and Asia, respectively, in the Northern Hemisphere winter season. Compared to the evaporation maxima in the Northern Hemisphere tropics and subtropics, the maxima at the corresponding Southern Hemisphere latitudes are 40–50% weaker in the Southern Hemisphere summer season.

[20] In the Northern (Southern) Hemisphere spring (autumn) season (March-April-May; Figure 2b), the Northern Hemisphere evaporation maxima, especially over the Gulf Stream and the Kuroshio, begin to weaken and the Southern Hemisphere maxima begin to strengthen. In June-July-August (Figure 2c), the Northern (Southern) Hemisphere maxima are at their weakest (strongest), with the effects of the warm, Northern Hemisphere ocean currents becoming almost unnoticeable.

[21] There is considerably more evaporation in the Southern Hemisphere than in the Northern Hemisphere in September-October-November (Figure 2d). The well-known evaporation minimum near the equator and a strong, zonal, land-ocean gradient of evaporation near the west coast of South America and Africa are seen clearly in the GSSTF2 data set.

[22] As mentioned earlier, we estimated evaporation over land by combining the S05 EmP with the GPCP and GPROF precipitation estimates. The S05 EmP is shown in Figure 3, and the estimated evaporation over land is shown in Figure 4. Unlike the overocean evaporation in Figure 2, the overland evaporation has its maximum in the summer hemisphere. In December-January-February (Figures 4a and 4e), the overland evaporation has its maximum in South America, southern Africa, northern Australia, and the southern Maritime Continent. In these regions, the GPCP-derived overland evaporation (Figure 4a) is 2–3 mm/d less than the GPROF-derived overland evaporation (Figure 4e). In this season, evaporation over Northern Hemisphere land is confined to coastal regions and is approximately 1–2 mm/d.

[23] In March-April-May (Figures 4b and 4f), evaporation over land begins to move northward and inland from

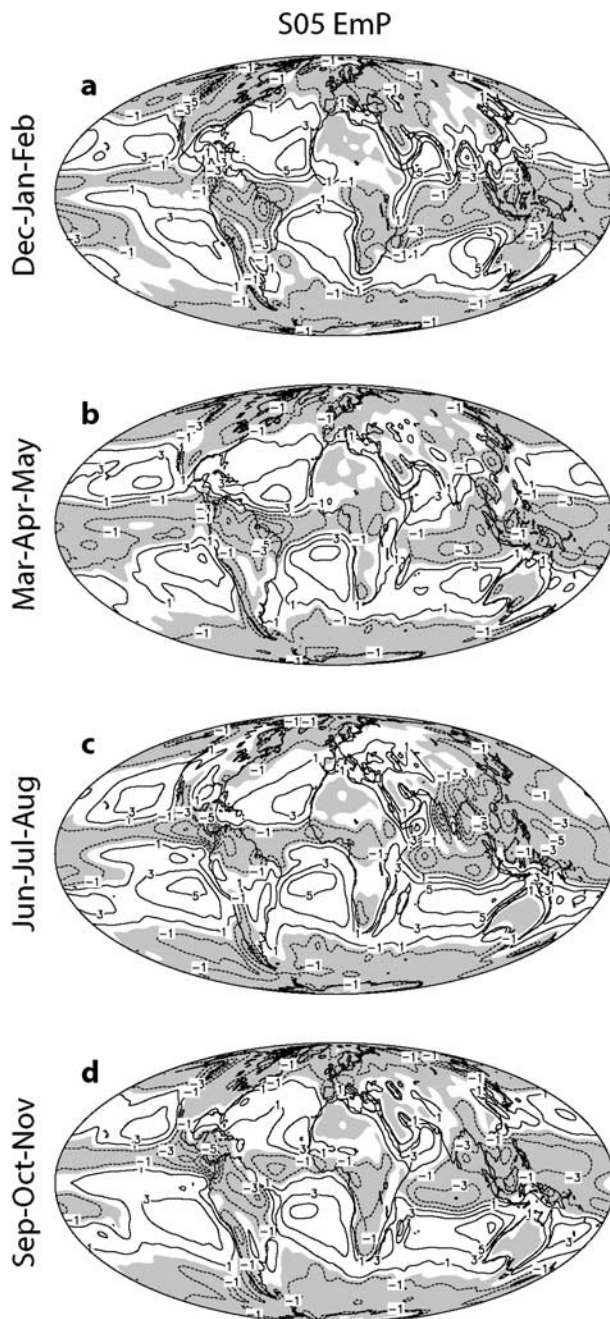


**Figure 3.** Average EmP during 1988–2000 from S05. (a) December–January–February, (b) March–April–May, (c) June–July–August, and (d) September–October–November. Negative contour values (dashed contours; shaded) are  $-7$  mm/d,  $-5$  mm/d,  $-3$  mm/d, and  $-1$  mm/d. Positive contour values (solid contours) are  $1$  mm/d,  $3$  mm/d,  $5$  mm/d, and  $7$  mm/d.

coastal regions in the Northern Hemisphere. The  $2$ – $3$  mm/d difference between the GPCP- and GPROF-derived, overland evaporation persists. In the Northern Hemisphere summer (June–July–August; Figures 4c and 4d), there are evaporation maxima over the southwest United States–northern Mexico, the North American Great Plains, central America, northern South America, tropical Africa, southern

Europe, central Asia, and southeast Asia. In these maxima, the GPROF-derived overland evaporation is approximately  $7$ – $9$  mm/d,  $1$ – $2$  mm/d more than the GPCP-derived overland evaporation. In September–October–November (Figures 4d and 4h), overland evaporation maxima move southward and resemble their March–April–May counterparts in locations and magnitudes.

## 5. Annual Cycle of Net Atmospheric Freshwater

[24] When the atmospheric water equation is integrated in a vertical column and over a few-month (one-season) period, the tendency term (the so-called storage term) is negligibly small compared to other terms because observations and model-based estimates show that the atmosphere cannot store water for longer than a few weeks. Therefore, of the remaining terms, the vertically integrated water flux divergence balances vertically integrated EmP. This balance allows us to interpret seasonally averaged EmP estimates as the net moisture flux divergence in the atmosphere.

[25] The EmP estimates over the oceans, derived by combining the GPCP and GPROF precipitation and the GSSTF2 evaporation estimates, are shown in Figure 5. Both groups of EmP estimates reflect similarities and differences between the GPCP and GPROF precipitation estimates and show generally similar features. In both groups, moisture flux convergences in the Atlantic and Pacific ITCZs are weakest in December–January–February (Figures 5a and 5e) and strongest in June–July–August (Figures 5c and 5g). On the basis of seasonal moisture transport estimates by *Trenberth and Guillemot* [1998] from the NCEP–NCAR reanalysis, the EmP distribution in Figure 5 can be interpreted as the Asian–Australian monsoon-related moisture flux convergences fed by moisture flux divergences out of the Arabian Sea–Bay of Bengal–southern Indian Ocean regions in December–January–February and out of the southern Indian Ocean–western Arabian Sea regions in June–July–August. The moisture precipitating over the Gulf Stream and the Kuroshio originates in the tropical–subtropical North Atlantic and North Pacific, respectively, in all seasons. The S05 EmP (Figure 3) shows generally weaker and broader moisture flux convergence and divergence regions compared to the satellite-based EmP estimates in Figure 5, suggesting that the global water cycle over the oceans is significantly less vigorous in the S05 estimate than in the satellite-based estimates.

## 6. Annual Fundamental Global Water Cycle

[26] As mentioned in the Introduction, the FGWC is driven by the annual cycle of solar irradiance and this cycle is primarily between the Northern and Southern Hemispheres because of the hemispheric asymmetry in solar irradiance. Therefore zonally averaged quantities important in the FGWC are described first in this section, followed by the hemispheric-averaged FGWC.

[27] Zonally averaged overocean evaporation from GSSTF2 and S05 EmP are shown in Figure 6; zonally averaged GPCP and GPROF precipitation estimates, the overocean EmP estimates derived from these two precipitation estimates and the GSSTF2 evaporation, and the overland evaporation estimates derived from the two precipitation

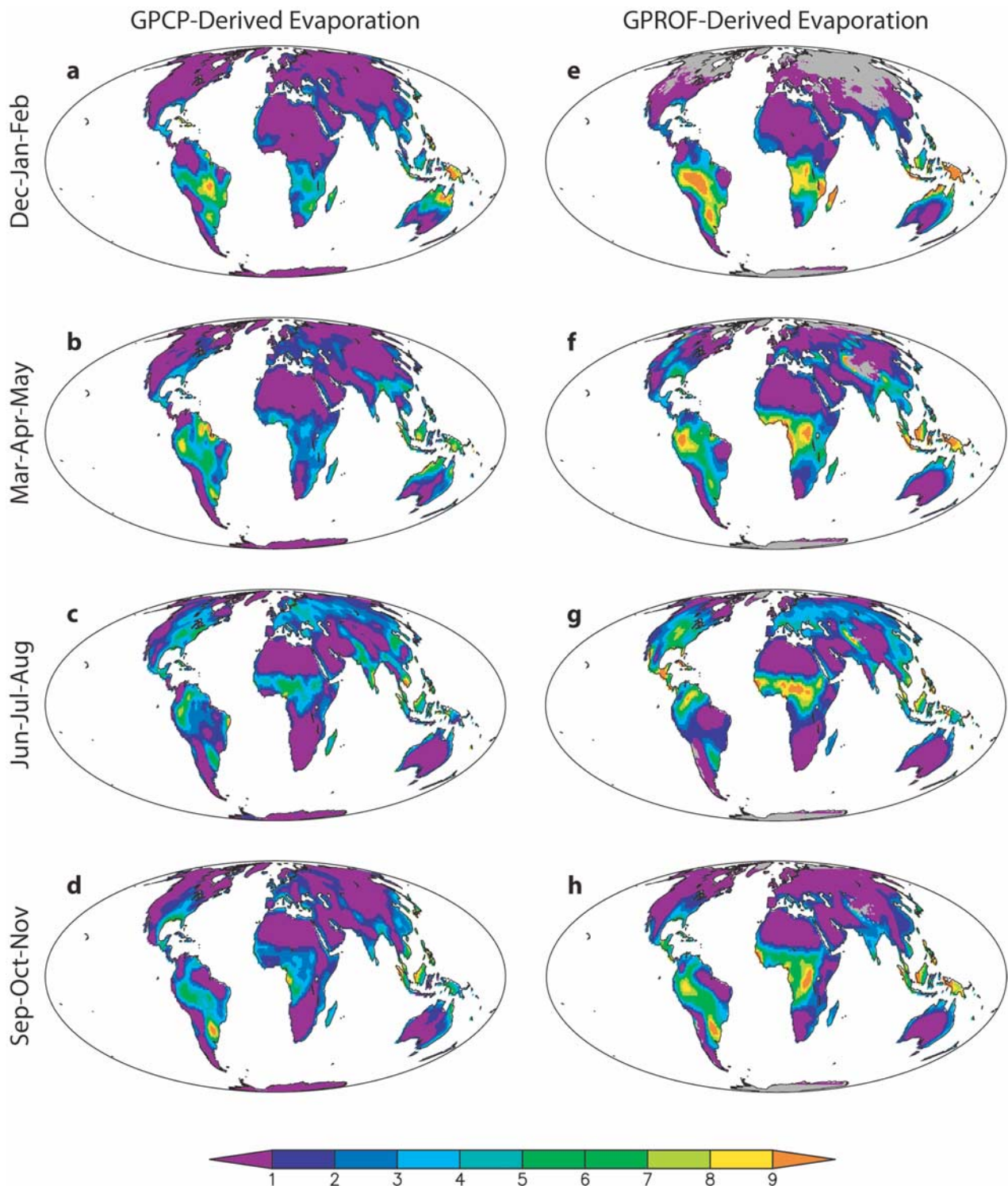


**Figure 4.** Average overland evaporation (mm/d) during 1988–2000 derived from GPCP and GPROF precipitation and S05 EmP. (a) GPCP; December-January-February. (b) GPCP; March-April-May. (c) GPCP; June-July-August. (d) GPCP; September-October-November. (e) GPROF; December-January-February. (f) GPROF; March-April-May. (g) GPROF; June-July-August. (h) GPROF; September-October-November.

estimates and the S05 EmP are also shown in Figure 6. In addition to the major, two-dimensional (longitude-latitude) features of these quantities described in the previous sections, Figure 6 also shows that the satellite-derived EmP extrema

are narrower compared to the S05 EmP extrema in their latitudinal extent. Also, tropical-subtropical precipitation maxima (minima) are associated with negative minima (positive maxima) in EmP. This relationship suggests that

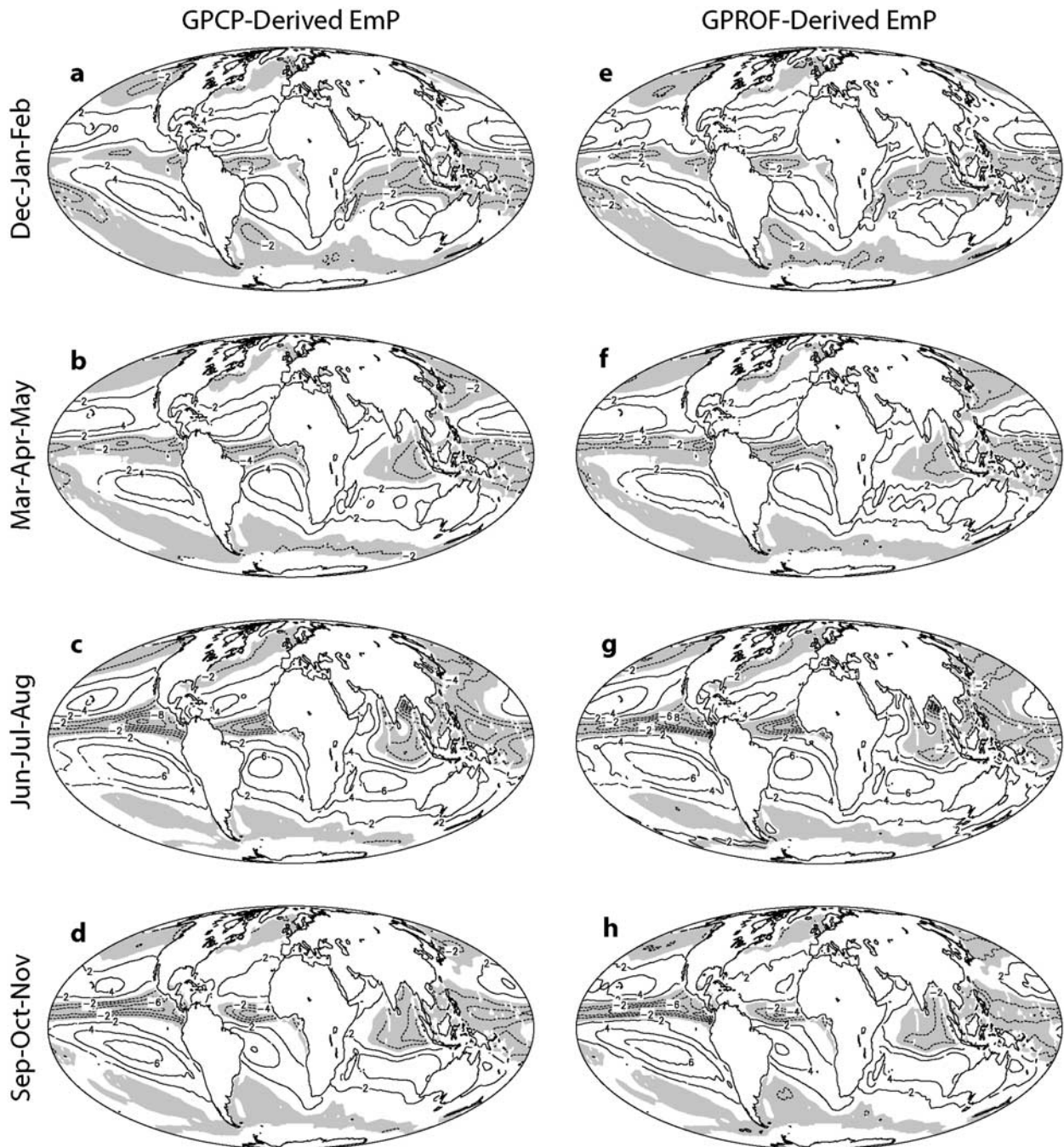


**Figure 5.** Average overocean EmP during 1988–2000 derived from GPCP and GPROF precipitation and GSSTF2 evaporation. (a) GPCP; December-January-February. (b) GPCP; March-April-May. (c) GPCP; June-July-August. (d) GPCP; September-October-November. (e) GPROF; December-January-February. (f) GPROF; March-April-May. (g) GPROF; June-July-August. (h) GPROF; September-October-November. Negative contour values (dashed contours; shaded) are  $-6$  mm/d,  $-4$  mm/d, and  $-2$  mm/d. Positive contour values (solid contours) are  $2$  mm/d,  $4$  mm/d, and  $6$  mm/d.

there is moisture flux divergence from the positive EmP maxima to supply moisture to precipitation regions in the same hemisphere as well as across the equator in the other hemisphere.

[28] The rates at which precipitation and evaporation process water over land and ocean in the Northern and Southern Hemispheres and the rate at which moisture flux is

transported from one hemisphere to the other in the GPCP- and GPROF-derived estimates are shown in Figure 7, and those in the truncated GPCP- and augmented GPROF-derived estimates are shown in Figure 8. Precipitation and evaporation rates are given as absolute values, and also as fractions of total hemispheric and global rates. All rate estimates are averaged over land and oceans by hemispheres



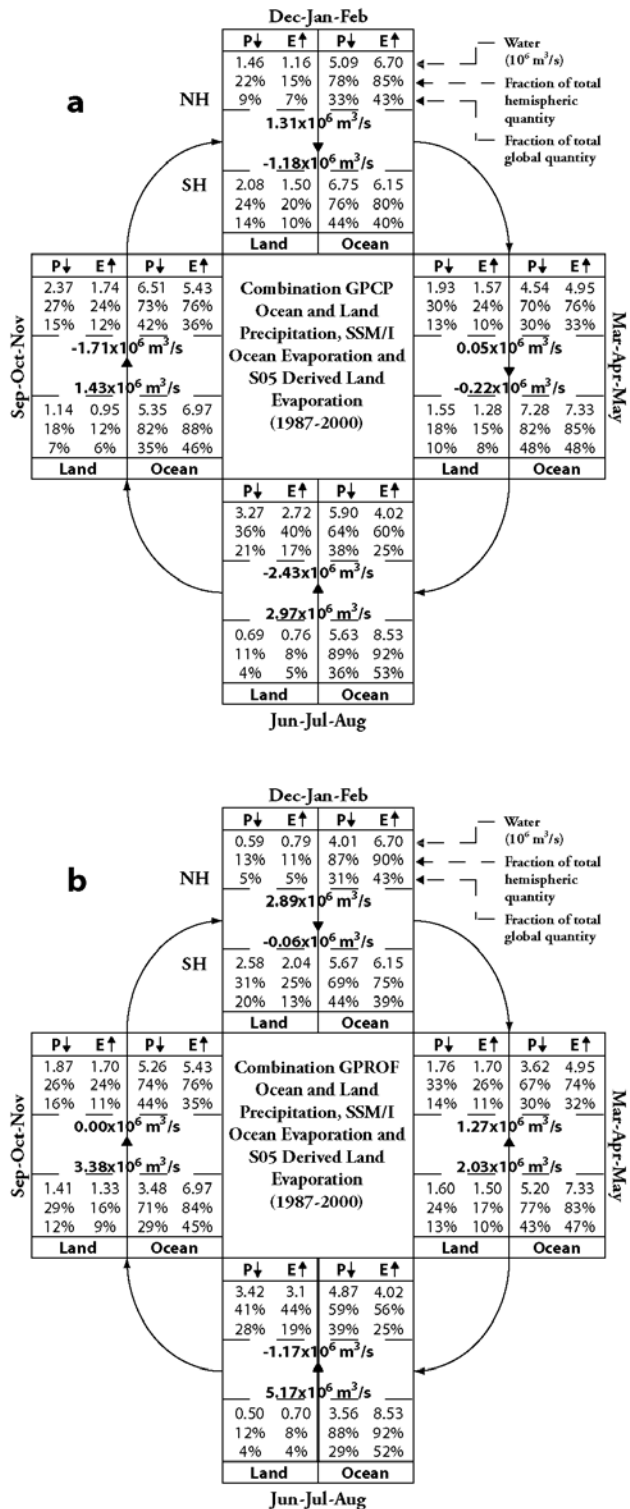


**Figure 7.** FGWC based on precipitation, GSSTF2 over-ocean evaporation, and overland evaporation based on combined S05 EmP and GPCP and GPROF precipitation during 1988–2000. Arrows and numbers across the hemispheric interface denote the direction and amount of net moisture flux transport. All quantities are in units of  $10^6 \text{ m}^3 \text{ s}^{-1}$ . (a) GPCP-based FGWC and (b) GPROF-based FGWC.

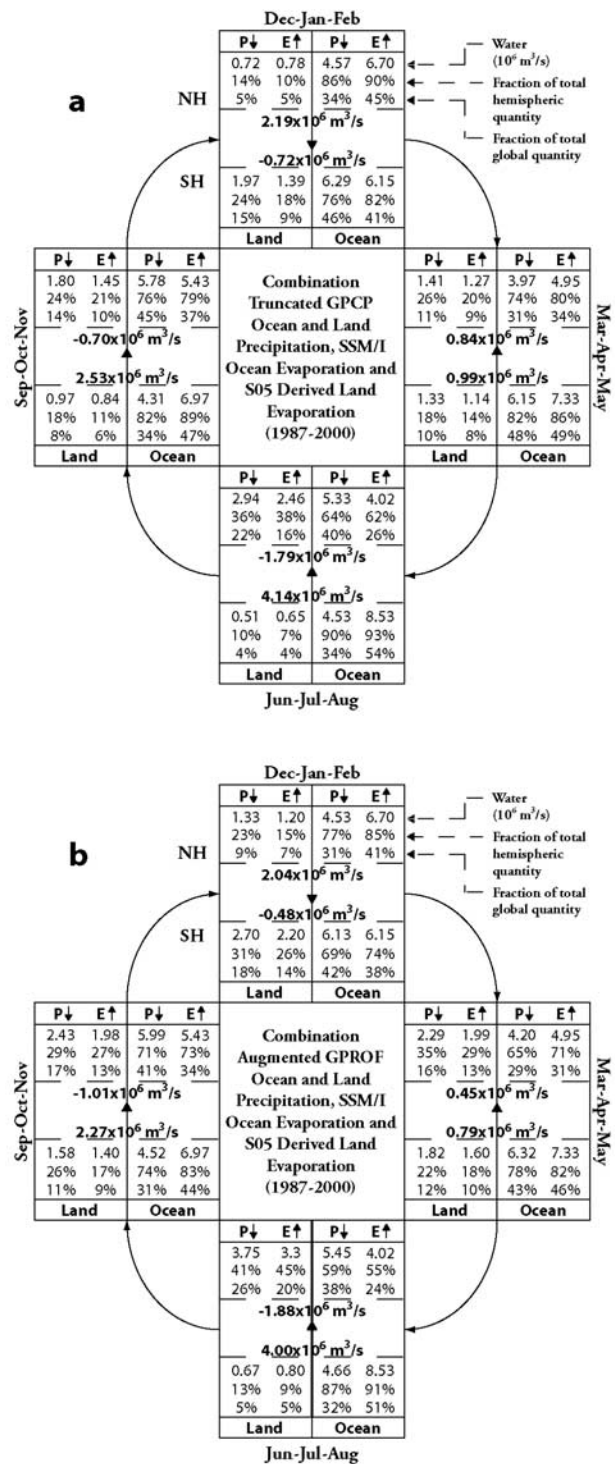


**Figure 8.** FGWC based on precipitation, GSSTF2 over-ocean evaporation, and overland evaporation based on combined S05 EmP and GPCP and GPROF precipitation during 1988–2000. Arrows and numbers across the hemispheric interface denote the direction and amount of net moisture flux transport. All quantities are in units of  $10^6 \text{ m}^3 \text{ s}^{-1}$ . (a) Truncated GPCP-based FGWC and (b) augmented GPROF-based FGWC.

**Table 2.** Net, Annual, Hemispheric Import/Export of Atmospheric Moisture in the FGWC Estimated Using Four Remote-Sensing-Based Precipitation Data Sets During 1988–2000<sup>a</sup>

|                 | Northern Hemisphere | Southern Hemisphere |
|-----------------|---------------------|---------------------|
| GPCP            | −2.78               | 3.00                |
| GPROF           | 2.99                | 10.52               |
| Truncated GPCP  | 0.54                | 6.94                |
| Augmented GPROF | −0.40               | 6.58                |

<sup>a</sup>Values are given in  $10^6 \text{ m}^3 \text{ s}^{-1}$ . Negative (positive) sign denotes import (export).

and seasons. The seasonal-average net EmP, interpreted as moisture flux divergence and converted to moisture volume transport, for each hemisphere and season is also given in Figures 7 and 8. Seventy-five to 85% of the total global evaporation occurs over the oceans in each season and the rest occurs over land. Therefore overocean evaporation is the dominant source of atmospheric moisture in the FGWC. As described earlier, maximum overocean (overland) evaporation occurs in the winter (summer) hemisphere; this phase difference is largely due to the very different heat capacities and the consequent response times of ocean and land. In transition seasons (March–April–May and September–October–November), there is much more overocean evaporation in the Southern Hemisphere than in the Northern Hemisphere. Approximately 70% of the total global precipitation in all four estimates in Figures 7 and 8 in each season occurs over the ocean and approximately 30% occurs over land. The overland precipitation has its maximum in Northern Hemisphere summer (June–July–August) in all four estimates.

[29] Figures 7 and 8 also show that there is a net moisture transport from the winter hemisphere to the summer hemisphere in December–January–February and June–July–August in all four FGWC estimates. While the net moisture transport is from the Southern to the Northern Hemisphere in September–October–November in all four FGWC estimates, the transport is from the Northern to Southern Hemisphere in March–April–May in the GPCP-derived FGWC estimates whereas it is from the Southern to the Northern Hemisphere in the other three FGWC estimates. The net annual, hemispheric moisture imports/exports in the four FGWC estimates are shown in Table 2. All four estimates in Table 2 show a net moisture export from the Southern to the Northern Hemisphere, but only the GPCP-derived import and export are closely balanced at approximately  $3 \times 10^6 \text{ m}^3 \text{ s}^{-1}$ . Since errors in any of these EmP estimates are not known, it can be concluded that the Southern Hemisphere export matches the Northern Hemisphere import in the GPCP-derived, net annual FGWC, but not in the other three FGWC. These results and their implications are discussed in the next section.

## 7. Discussion and Conclusions

[30] We used remote-sensing-based, blended microwave–infrared–rain gauge (GPCP) and passive microwave only (GPROF), precipitation estimates; remote-sensing-based, passive microwave (GSSTF2), overocean evaporation estimates; and EmP produced by the National Center for Atmospheric Research/Climate Analysis Section (D. P.

Stepaniak, Vertically integrated mass, moisture heat, and energy budget products derived from the NCEP/NCAR reanalysis, available online at <http://www.cgd.ucar.edu/cas/catalog/newbudgets/>; S05) to address the questions posed in the Introduction about the average annual cycle of the atmospheric branch of the FGWC. The results show that (1) 75 to 85% of the total global evaporation and approximately 70% of the total global precipitation occur over the oceans in each season; (2) in the GPCP-based FGWC estimate, the dominant cross-equatorial atmospheric moisture transports in the atmospheric branch of the FGWC supply a significant amount of moisture to precipitation regions and are from the Northern Hemisphere to the Southern Hemisphere in December–January–February and the Southern Hemisphere to the Northern Hemisphere in June–July–August, with an approximately  $3 \times 10^6 \text{ m}^3 \text{ s}^{-1}$  net, annual transport from the Southern Hemisphere to the Northern Hemisphere; (3) GPCP and GPROF precipitation estimates have generally similar magnitudes, except in the tropical Africa, North Atlantic, and North American monsoon regions, where the GPROF precipitation is approximately twice as much as the GPCP precipitation; moreover, the GPROF precipitation maxima are generally more localized in space; (4) the overocean evaporation maxima in the GSSTF2 data set are located in the winter hemisphere, whereas the overland evaporation estimated from the S05 EmP and the GPCP and GPROF precipitation have maxima in the summer hemisphere; and (5) the global water cycle over the oceans is less vigorous in the S05 EmP than in the satellite-based estimates.

[31] The apparent internal consistency of the GPCP-based FGWC estimates in Figure 7 is remarkable since they were derived from three independent data sets (GPCP precipitation, GSSTF2 overocean evaporation, and overland evaporation from the GPCP precipitation and the S05 EmP). The substantial imbalances in GPROF-, truncated GPCP-, and augmented GPROF-derived interhemispheric moisture transports show that while missing precipitation data at middle and high latitudes in GPROF are important in the FGWC, the augmentation of missing GPROF precipitation data by GPCP precipitation data to fill in missing data still leaves a substantial imbalance in the augmented GPROF-derived FGWC. This internal inconsistency even in the augmented GPROF-derived FGWC may be due to inadequate diurnal samples in GPROF precipitation, which might produce more accurate, instantaneous precipitation rates but increase errors in monthly and longer-term average precipitation rates. In addition, it is well known that GPROF estimates are less accurate over land as they are heavily dependent on 85 GHz brightness temperatures which do not always succeed in capturing rain events [Kummerow *et al.*, 1996] over land. As discussed by Kummerow *et al.* [2001], GPROF also has biases in precipitation estimates compared to surface rain gauge and radar measurements. The bias in monthly  $5^\circ$  grids over land is +17% compared to the GPCC rain gauge network. Over oceans, the bias in monthly  $2.5^\circ$  grids is found to be within −9% to +6% when compared to atoll gauges.

[32] The approximately  $3 \times 10^6 \text{ m}^3 \text{ s}^{-1}$  export/import of atmospheric moisture in the GPCP-derived results is approximately 0.9–1 mm/d in moisture flux divergence. This is several times more than 0.11 mm/d estimated by

*Peixoto and Oort* [1983] and 0.22 mm/d estimated by *Chen et al.* [1995], and approximately 0.0 mm/d in S05; which of these four estimates is closest to the true cross-equatorial moisture flux divergence in nature? All data used in these three studies have unknown errors, therefore it is not currently possible to estimate errors in any of the three cross-equatorial moisture flux divergence estimates. It is likely, however, that *Peixoto and Oort's* [1983] 10 years' radiosonde-based estimate was highly inaccurate because of large uncertainties in estimating large-scale winds and atmospheric humidity, especially over the oceans. *Chen et al.'s* [1995] moisture flux divergence estimate was derived from 2 years' HIRS2/MSU-based precipitation estimates, which were derived from radiances assimilated in an atmospheric general circulation model, and the NMC GDAS upper-air data; problems in the latter are discussed by *Trenberth and Olson* [1988] and *Chen et al.* [1995]. While S05 is an improvement over the original NCEP-NCAR reanalysis moisture flux divergence, it is not clear whether the perfect balance in net moisture flux divergence is natural or forced by the assimilation process of the S05 improvement process. The present study provides a longer-term (13 years) estimate of the FGWC, based primarily on remote sensing which enables a better observational coverage of precipitation and evaporation over oceans compared to the previous studies. Similarly, the S05 EmP used in the present study is probably more accurate compared to EmP from the NMC GDAS. Therefore we believe that the FGWC estimated in the present study is likely to be more accurate. The differences in FGWC based on the two precipitation products (GPCP and GPROF), however, raises a crucial question about error estimates in each individual product. As pointed out by the PIP studies, it is possible that characteristics of the various precipitation products may be quantitatively different at various timescales.

[33] It is not necessary that there should be any constraint on ocean currents to transport the approximately  $3 \times 10^6 \text{ m}^3 \text{ s}^{-1}$  net Southern-Hemisphere-to-Northern-Hemisphere freshwater transported by winds back to its source regions in the Southern Hemisphere within 1 year as assumed by *Chen et al.* [1995]. Therefore there is potential for sea surface salinity (SSS) in the southern oceans to increase and for SSS in major precipitation regions in the Northern Hemisphere to decrease in response to this net freshwater transport in the atmosphere. This may be one of the causes of climatological SSS to be higher in southern oceans than in northern oceans [see, e.g., *Levitus et al.*, 1994]. In addition, experiments with a global ocean general model, forced by EmP derived from GPCP precipitation and GSSTF2 evaporation for 1988 to 2000, show that SSS increased approximately 0.4–0.6 practical salinity units in the EmP source regions in the southern Indian and southern Pacific Oceans during 1995–2000 compared to 1988–1994 [*Huang and Mehta*, 2004, 2005]. These experiments also show that the SSS and density gradients created by the net freshwater transport in the FGWC can generate interannual and longer timescale ocean circulation and heat transport changes, potentially causing changes in sea surface temperature and climate. Moreover, as the results reported here show, the overocean components of the atmospheric branch of the FGWC are very important and can be affected by ocean dynamics-thermodynamics and ocean-atmosphere

interactions. Therefore the oceans' role in the FGWC is very important and should be a significant component in the Global Energy and Water Cycle Experiment, International Geosphere Biosphere Program, and other national and international research programs on the global water cycle.

[34] **Acknowledgments.** This research was supported by NASA grants NAG5-11785 and NAG5-12729. The authors thank G. Huffman and E. Nelkin for their help in obtaining precipitation data sets. The GPCP combined precipitation data were developed and computed by the NASA Goddard Space Flight Center's Laboratory for Atmospheres as a contribution to the GEWEX Global Precipitation Climatology Project. The authors also thank D. Stepaniak for clarifying the technique used in the NCAR/CAS EmP data. Discussions with E. Smith and B. Huang are gratefully acknowledged.

## References

- Adler, R. F., C. Kidd, G. Petty, M. Morrissey, and H. M. Goodman (2001), Intercomparison of global precipitation products: The third Precipitation Intercomparison Project (PIP-3), *Bull. Am. Meteorol. Soc.*, **82**, 1377–1396.
- Adler, R. F., et al. (2003), The Version-2 Global Precipitation Climatology Project (GPCP) monthly precipitation analysis (1979–present), *J. Hydro-meteorol.*, **4**, 1147–1167.
- Arkin, P. A., and B. N. Meisner (1987), The relationship between large-scale convective rainfall and cold cloud over the Western Hemisphere during 1982–1984, *Mon. Weather Rev.*, **115**, 51–74.
- Atlas, R., R. N. Hoffman, S. C. Bloom, J. C. Jusem, and J. Ardizzone (1996), A multiyear global surface wind velocity dataset using SSM/I wind observations, *Bull. Am. Meteorol. Soc.*, **77**, 869–882.
- Barrett, E. C., et al. (1994), The first WETNET Precipitation Intercomparison Project: Intercomparison of results, *Remote Sens. Rev.*, **11**, 303–373.
- Bauer, P., L. Schanz, R. Bennartz, and P. Schlüssel (1998), Outlook for combined TMI-VIRS algorithms for TRMM: Lessons from the PIP and AIP projects, *J. Atmos. Sci.*, **55**, 1714–1729.
- Chen, T.-C., and J. Pfaendtner (1993), On the atmospheric branch of the hydrological cycle, *J. Clim.*, **6**, 161–167.
- Chen, T.-C., J. Pfaendtner, and S.-P. Weng (1994), Aspects of the hydrological cycle of the ocean-atmosphere system, *J. Phys. Oceanogr.*, **24**, 1827–1833.
- Chen, T.-C., J.-M. Chen, and J. Pfaendtner (1995), Low-frequency variations in the atmospheric branch of the global hydrological cycle, *J. Clim.*, **8**, 92–107.
- Chou, S.-H. (1993), A comparison of airborne eddy correlation and bulk aerodynamic methods for ocean-air turbulent fluxes during cold-air outbreaks, *Boundary Layer Meteorol.*, **64**, 75–100.
- Chou, S.-H., R. Atlas, C. Shie, and J. Ardizzone (1995), Estimates of surface humidity and latent heat fluxes over oceans from SSM/I data, *Mon. Weather Rev.*, **123**, 2405–2418.
- Chou, S.-H., C.-L. Shie, R. M. Atlas, and J. Ardizzone (1997), Air-sea fluxes retrieved from Special Sensor Microwave Imager data, *J. Geophys. Res.*, **102**, 12,705–12,726.
- Chou, S.-H., E. Nelkin, J. Ardizzone, R. M. Atlas, and C.-H. Shie (2003), Surface turbulent heat and momentum fluxes over global oceans based on the Goddard Satellite Retrievals, Version 2 (GSSTF2), *J. Clim.*, **16**, 3256–3273.
- Clayson, C. A., and J. A. Curry (1996), Determination of surface turbulent fluxes for the Tropical Ocean-Global Atmosphere Coupled Ocean-Atmosphere Response Experiment: Comparison of satellite retrievals and in situ measurements, *J. Geophys. Res.*, **101**, 28,515–28,528.
- Clayson, C. A., C. W. Fairwall, and J. A. Curry (1996), Evaluation of turbulent fluxes at the ocean surface using surface renewal theory, *J. Geophys. Res.*, **101**, 28,503–28,513.
- Huang, B., and V. M. Mehta (2004), Response of the Indo-Pacific warm pool to interannual variations in net atmospheric freshwater, *J. Geophys. Res.*, **109**, C06022, doi:10.1029/2003JC002114.
- Huang, B., and V. M. Mehta (2005), Response of the Pacific and Atlantic oceans to interannual variations in net atmospheric freshwater, *J. Geophys. Res.*, **110**, C08008, doi:10.1029/2004JC002830.
- Huffman, G. J., R. F. Adler, P. Arkin, A. Chang, R. Ferraro, A. Gruber, J. Janowiak, A. McNab, B. Rudolf, and U. Schneider (1997), The Global Precipitation Climatology Project (GPCP) Combined Precipitation Dataset, *Bull. Am. Meteorol. Soc.*, **78**, 5–20.
- Joyce, R., and P. A. Arkin (1997), Improved estimates of tropical and subtropical precipitation using the GOES precipitation index, *J. Atmos. Oceanic Technol.*, **14**, 997–1011.
- Kalnay, E., et al. (1996), The NCEP-NCAR 40-year reanalysis project, *Bull. Am. Meteorol. Soc.*, **77**, 437–471.

- Kummerow, C., O. S. Olson, and L. Giglio (1996), A simplified scheme for obtaining precipitation and vertical hydrometeor profiles from passive microwave sensors, *IEEE Trans. Geosci. Remote Sens.*, *34*, 1213–1232.
- Kummerow, C., et al. (2001), The evolution of the Goddard Profiling algorithm (GPROF) for rainfall estimation from passive microwave sensors, *J. Appl. Meteorol.*, *40*, 1801–1820.
- Levitus, S., R. Burgett, and T. Boyer (1994), *World Ocean Atlas 1994*, vol. 3, *Nutrients*, NOAA Atlas NESDIS 3, U.S. Dep. of Commer., Washington, D. C.
- Peixóto, J. P., and A. H. Oort (1983), The atmospheric branch of the hydrological cycle and climate, in *Variations in the Global Water Budget*, edited by A. Street-Perrott, M. Beran, and R. Ratcliffe, pp. 5–65, Springer, New York.
- Rodda, J. C. (1995), Capturing the hydrologic cycle, in *Time and the River*, edited by G. W. Kite, pp. 25–58, Water Resour. Publ., Highlands Ranch, Colo.
- Schlüssel, P. (1996), Satellite remote sensing of evaporation over sea, in *Radiation and Water in the Climate System: Remote Measurements*, edited by E. Raschke, chap. 16, pp. 431–461, Springer, New York.
- Schlüssel, P., L. Schanz, and G. English (1995), Retrieval of latent heat flux and longwave irradiance at the sea surface from SSM/I and AVHRR measurements, *Adv. Space Res.*, *16*(10), 107–116.
- Schulz, J., J. M. Meywerk, S. Ewald, and P. Schlüssel (1997), Evaluation of satellite-derived latent heat fluxes, *J. Clim.*, *10*, 2782–2795.
- Smith, E. A., et al. (1998), Results of WetNet PIP-2 project, *J. Atmos. Sci.*, *55*, 1483–1536.
- Sohn, B. J., E. A. Smith, F. R. Robertson, and S.-C. Park (2004), Derived overocean water vapor transports from satellite-derived E-P datasets, *J. Clim.*, *17*, 1352–1365.
- Trenberth, K. E., and C. J. Guillemot (1998), Evaluation of the atmospheric moisture and hydrological cycle in the NCEP/NCAR reanalyses, *Clim. Dyn.*, *14*, 213–231.
- Trenberth, K. E., and J. G. Olson (1988), An evaluation and intercomparison of global analyses from NMC and ECMWF, *Bull. Am. Meteorol. Soc.*, *69*, 1047–1057.
- Trenberth, K. E., and D. P. Stepaniak (2003a), Covariability of components of poleward atmospheric energy transports on seasonal and interannual timescales, *J. Clim.*, *16*, 3691–3705.
- Trenberth, K. E., and D. P. Stepaniak (2003b), Seamless poleward atmospheric energy transports and implications for the Hadley circulation, *J. Clim.*, *16*, 3706–3722.

---

A. J. DeCandis and V. M. Mehta, Center for Research on the Changing Earth System, 10211 Wincopin Circle, Suite 240, Columbia, MD 21044, USA. (vikram@crces.org; decandis@crces.org)

A. V. Mehta, NASA Goddard Space Flight Center, Code 912.1, Greenbelt, MD 20771, USA. (amita@radar.gsfc.nasa.gov)